CHAPTER 3

Development of Mathematical Model for force prediction in Single Point Incremental Sheet Forming and Validation by Experiments & Simulation

3.1 Introduction

In this chapter, an attempt has been made to develop a mathematical model for prediction of forming forces in RAISF process. Sections 1.5 and 1.6 give a comprehensive review of works carried out in this field. It can be concluded from literature review that although several attempts have been made to develop a mathematical model of ISF, still a comprehensive model for force prediction has not been established. Further, most of the models are empirical in nature and they are used to calculate average force during the process. Some other models consider only plane stresses in thickness, meridional and circumferential direction without considering the shear stresses. Very few works have been done considering all the six stress components to finally arrive at forces. In the current work, a simple mathematical model for the ISF process has been developed in a cylindrical coordinate system considering all the stress components. All force components have been calculated at different forming depths where tool moves in different radii. Axial force component and vector diagram of forces appearing in the plane of undeformed sheet during the RAISF have been shown in Figure 3.1(a), (b) and (c).

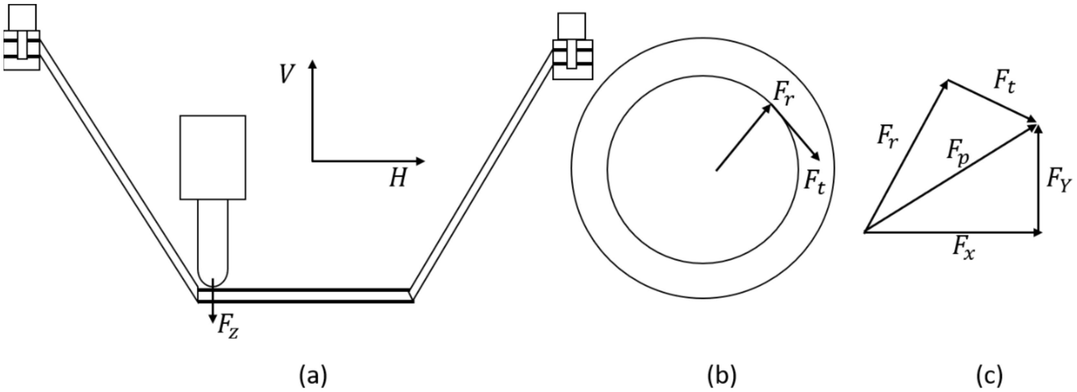

Figure 3.1: (a) Schematic diagram of ISF (b) Forming forces in plane of undeformed sheet (c) Vector diagram of forming forces in plane of undeformed sheet

The obtained results have been compared with the FEA model developed using the ABAQUS platform. Finally, experiments have been performed on aluminium alloy 6061 on six axis industrial robotic arm with similar experimental conditions as used for analytical and FEA model. Different force components were measured using dynamometer, mounted on the robotic arm. The obtained results for various force components and total force have been compared.

3.2 Mathematical model development

For solving the mathematical equations, cylindrical 3D coordinate has been chosen as tool motion to gives a conical shape, and that can be easily replicated in this co-ordinate system. The center of the undeformed sheet has been chosen as the origin of the global coordinate system. The element has been taken in a local 3D polar co-ordinate system which is at a forming depth h and of length r*dθ in the radial direction at an angle θ in the circumferential direction on the surface of the sheet in contact with the tool in the local polar co-ordinate system, as shown in Figure 3.2 (a) and (b). It is worth noting that the three directions; radial (r-direction), circumferential (θ-direction), and axial (z-direction) may not be necessarily the principal directions. Hence, all the six-stress components have been considered.

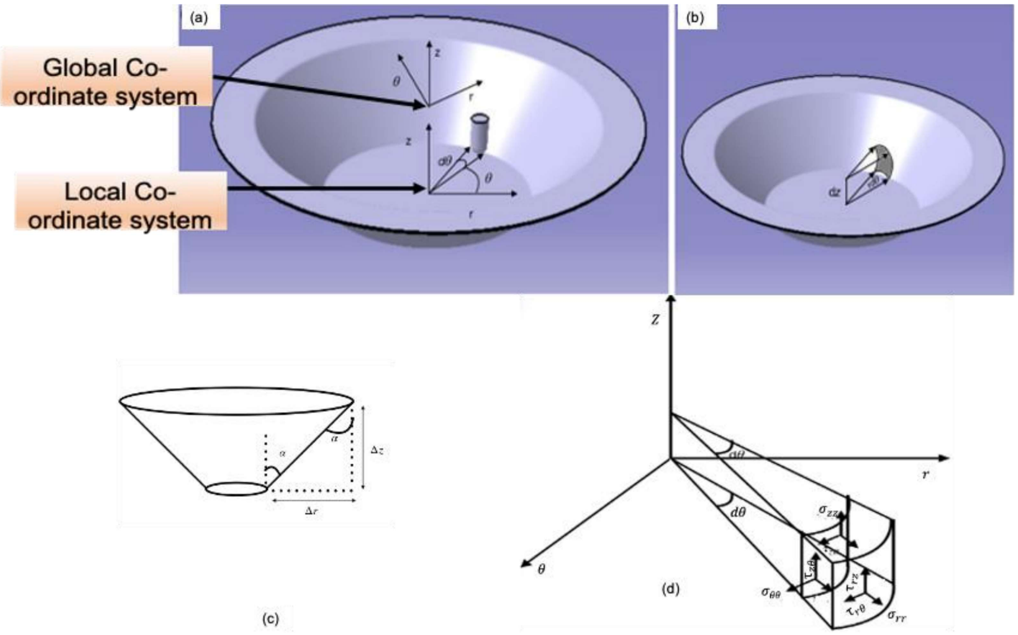

Figure 3.2: (a) Definition of 3D polar co-ordinate for considering an element, (b) Representation of taken element, (c) Definition of wall angle in terms of step depth, (d) Stresses acting on the taken element

The following assumptions had been made to develop the model.

1: All body forces have been neglected during the analysis.

2: $\tau_{\theta z}$ has been neglected throughout the analysis.

3: Normal stress in radial and z-directions are distributed in the same ratio as that of increments provided in these directions for forming fixed wall angle cone. $\frac{\partial r}{\partial z} = \tan\alpha$, $\frac{\sigma_{rr}}{\sigma_{zz}} = \tan\alpha$, where, α is the wall angle of the formed cone. The wall angle and step depths can be understood from Figure 3.2(c).

4: For a given radius in which the tool is moving, $\tau_{r\theta}$ varies only along θ direction. If the considered element is under static equilibrium, the equilibrium equations in the differential forms can be written directly [136]. The free-body diagram of considered element is presented in Figure 3.2(d). Neglecting body forces, the equilibrium equations in the respective directions are given below:

In radial direction

$$\frac{\partial \sigma_{rr}}{\partial r} + \frac{1}{r}\frac{\partial \tau_{r\theta}}{\partial \theta} + \frac{\sigma_{rr} - \sigma_{zz}}{r} + \frac{\partial \tau_{rz}}{\partial z} = 0 \qquad (1)$$

In circumferential direction

$$\frac{\partial \tau_{r\theta}}{\partial r} + \frac{1}{r}\frac{\partial \sigma_{\theta\theta}}{\partial_{\theta}} + \frac{2}{r}\tau_{r\theta} = 0 \qquad (2)$$

In z direction

$$\frac{\partial \tau_{rz}}{\partial r} + \frac{\tau_{rz}}{r} + \frac{1}{r}\frac{\partial \tau_{\theta z}}{\partial \square} + \frac{\partial \sigma_{zz}}{\partial z} = 0 \qquad (3)$$

The major shear component has been assumed to act only along the radial direction only. Hence $\tau_{\theta z}$ has been neglected throughout the model. Further, from membrane analysis it can be said

$$\tau_{rz} = f\sigma_{rr}, \qquad (4)$$

Using the membrane analysis (4), equation (1) becomes

$$\frac{\partial \sigma_{rr}}{\partial_{r}} + \frac{1}{r}\frac{\partial \tau_{r\theta}}{\partial \theta} + \frac{\sigma_{rr} - \sigma_{\theta\theta}}{r} + f\frac{\partial \sigma_{rr}}{\partial z} = 0 \qquad (5)$$

With membrane analysis (4) and the assumption 2, equation (3) becomes

$$f\frac{\partial \tau_{rr}}{\partial_{r}} + f\frac{\partial_{rr}}{r} + \frac{\partial \sigma_{zz}}{\partial z} = 0 \qquad (6)$$

For any incremental sheet forming, the fabrication of 3D shapes is done by moving the tool over the sheet and providing increments to the tool, so that it can perform fabrication in different passes. For fabricating a conical wall, the increments are provided in the vertical and horizontal directions. In the current work, the increments are provided in the radial and vertically downward directions. These increments are generally small in comparison to r, and if the given assumption holds, then it can be assumed that on neglecting spring back:

$\triangle z = \triangle r \tan\alpha$, where $\triangle z$ is increment in the vertical direction and $\triangle r$ is increment in radial direction. If these are small then:

$$\partial r \, tan\alpha = \partial z \qquad (7)$$

Using assumption 3, it can be said that normal stress in radial and z-directions are distributed in the same ratio as that of increments:

$$\sigma_{rr} \, tan\alpha = \sigma_{zz} \qquad (8)$$

Taking differentials on both the sides,

$$\partial\sigma_{rr} \, tan\theta = \partial\sigma_{zz} \qquad (9)$$

From *(7)* and *(9)* it can be seen that

$$\frac{\partial\sigma_{rr}}{\partial r} = \frac{\partial\sigma_{zz}}{\partial z} \qquad (10)$$

Using equation *(10),* equation *(6)* further converges to

$$f\frac{\partial\sigma_{rr}}{\partial r} + f\frac{\sigma_{rr}}{r} + \frac{\partial\sigma_{rr}}{\partial r} = 0 \qquad (11)$$

$$\frac{\partial\sigma_{rr}}{\partial r}(1+f) = -f\frac{\sigma_{rr}}{r} \qquad (12)$$

Taking integrals on both sides of *(12)*

$$\int \frac{\partial\sigma_{rr}}{\sigma_{rr}} = \int \frac{\partial r}{r}\left\{\frac{-f}{1+f}\right\}$$

$$ln\,\sigma_{rr} = lnr^{\frac{-f}{1+f}} + ln\,C \qquad (13)$$

$$\sigma_{rr} = \frac{c}{r^{\frac{f}{1+f}}} \qquad (14)$$

From the above analysis, it is evident that for one complete cycle, the stress in the radial direction is constant. The analysis was performed on ABAQUS V6.13 with same parameters as used for the analytical model and considering the element when the instantaneous radius of the undeformed part is 82.5 mm, RMS value of the S_{11} was found to be approximately equal to 140 MPa as shown in Figure 3.3(a) and (b).

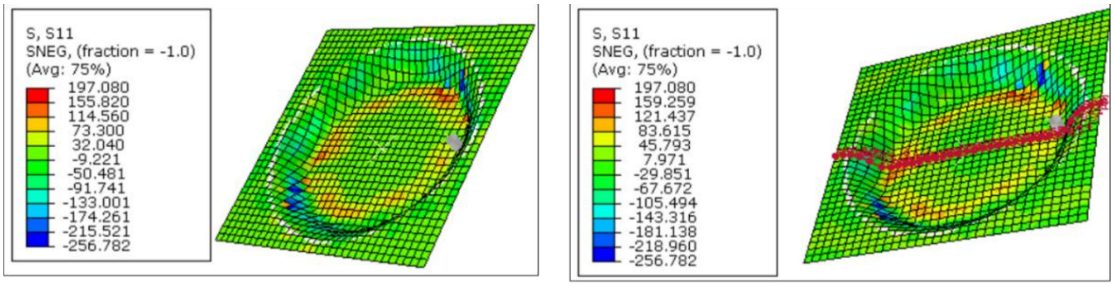

(a) (b)

Figure 3.3: Results obtained on abaqus (a) Radial stress distribution at radius of 82.5 mm and (b) Chosen path on the radial line for stress distribution.

For f $= \frac{1}{\sqrt{3}}$, C = 292.5

$$\sigma_{rr} = \frac{292.5}{r^{0.1667}} \tag{15}$$

Since σ_{rr} depends on instantaneous circle radius only, hence

$$\frac{\partial\sigma_{rr}}{\partial z} = 0 \tag{16}$$

From equilibrium equation in r-direction,

$$\frac{\partial\sigma_{rr}}{\partial r} + \frac{1}{r}\frac{\partial\tau_{r\theta}}{\partial\theta} + \frac{\sigma_{rr}-\sigma_{\theta\theta}}{r} + \frac{\partial\sigma_{rr}}{\partial z} = 0 \tag{17}$$

Using equation *(16)* and *(17)*

$$\frac{\partial}{\partial r}\left\{\frac{C}{r^{\frac{f}{1+f}}}\right\} + \frac{1}{r}\frac{\partial\tau_{r\theta}}{\partial\theta} + \frac{C}{r\left(r^{\frac{f}{1+f}}\right)} = \frac{\sigma_{\theta\theta}}{r} \tag{18}$$

Using equation *(17)*

$$\sigma_{rr}\left\{1 - \frac{f}{f+1}\right\} + \frac{\partial\tau_{r\theta}}{\partial\theta} = \sigma_{\theta\theta} \tag{19}$$

$$\frac{\partial\tau_{r\theta}}{\partial\theta} = \sigma_{\theta\theta} - \frac{\sigma_{rr}}{(1+f)} \tag{20}$$

In circumferential direction, with assumption 4, the equation in the circumferential direction converges to

$$\frac{1}{r}\frac{\partial\sigma_{\theta\theta}}{\partial_{\theta}} + \frac{2}{r}\tau_{r\theta} = 0 \tag{21}$$

$$\frac{\partial \sigma_{\theta\theta}}{\partial \theta} = -2\tau_{r\theta} \qquad (22)$$

From equations 20 and 22,

$$\frac{\partial \tau_{r\theta}}{\partial \sigma_{\theta\theta}} = \left(\frac{\sigma_{\theta\theta} - \frac{\sigma_{rr}}{(1+f)}}{2\tau_{r\theta}} \right)$$

$$2\int \tau_{r\theta}\, \partial\tau_{r\theta} = -\int \sigma_{\theta\theta}\, \partial\sigma_{\theta\theta} + \frac{\sigma_{rr}}{(1+f)} \int \partial\sigma_{\theta\theta} \qquad (23)$$

$$(\tau_{r\theta})^2 = \frac{\sigma_{rr}\sigma_{\theta\theta}}{(1+f)} - \frac{(\sigma_{\theta\theta})^2}{2} + k' \qquad (24)$$

If $\sigma_{\theta\theta} = 0, \tau_{r\theta} = 0,\ k' = 0$

$$(\tau_{r\theta})^2 = \sigma_{\theta\theta} \left\{ \frac{\sigma_{rr}}{(1+f)} - \frac{\sigma_{\theta\theta}}{2} \right\} \qquad (25)$$

From Von-Mises criteria,

$$(\sigma_{rr} - \sigma_{\theta\theta})^2 + (\sigma_{rr} - \sigma_{zz})^2 + (\sigma_{\theta\theta} - \sigma_{zz})^2 + 6[{\tau_{r\theta}}^2 + {\tau_{rz}}^2 + {\tau_{\theta z}}^2] = \bar{\sigma}^2 \qquad (26)$$

The model is valid for all wall angles; however, for validation purpose 45^0 wall angle has been chosen because of its simplicity.$\theta = 45^0, \sigma_{rr} = \sigma_{zz}, \tau_{\theta z} = 0$

$$2(\sigma_{rr} - \sigma_{\theta\theta})^2 + 6[{\tau_{r\theta}}^2 + f^2{\sigma_{rr}}^2] = \bar{\sigma}^2 \qquad (27)$$

$${\sigma_{rr}}^2(2 + 6f^2) - {\sigma_{\theta\theta}}^2 + \sigma_{\theta\theta}\sigma_{rr}\left(\frac{2-4f}{1+f}\right) = \bar{\sigma}^2 \qquad (28)$$

If one considers the strain to be acting from bending and stretching only [137], then from volume conservation

$$\varepsilon_\theta + \varepsilon_r + \varepsilon_f = 0 \qquad (29)$$

Total bending strain can be given by $ln\left(\frac{r_{tool}}{R_m}\right)$

Whereas total tensile strain can be given as, $\varepsilon_{stretching} = ln\left(\frac{t_0}{t}\right)$

Total strain can be given by $\varepsilon = ln\left(\frac{r_{tool}}{R_m}\frac{t_0}{t}\right)$ *(30)*

$$(\sigma_{rr})^2(2 + 6f^2) - {\sigma_{\theta\theta}}^2 + \sigma_{\theta\theta}\sigma_{rr}\left(\frac{2-4f}{1+f}\right) = \bar{\sigma}^2 \qquad (31)$$

From simple power law for annealed sheet, $\bar{\sigma} = K\varepsilon^n$. From tensile test K = 205 MPa, and n = 0.2

$$(\sigma_{rr})^2(2 + 6f^2) - \sigma_{\theta\theta}{}^2 + \sigma_{\theta\theta}\sigma_{rr}\left(\frac{2-4f}{1+f}\right) = K^2\left(\frac{4}{3}\right)\left[ln\frac{r_{tool}t_0}{R_m t}\right]^{2n} \qquad (32)$$

From the analytical model developed it can be said that the stress state appearing during the process is complex, but a few simple conclusions can be derived, as:

(a) The largest stress component is normal stress on the theta plane along the tool movement direction. Appreciable shear stress appears in the direction perpendicular to the tool motion along radial and z plane.

(b) From equation, it is clear that $\frac{\sigma_{rr}}{(1+f)} > \frac{\sigma_{\theta\theta}}{2}$. *(33)*

3.3 Contact area model

For contact area estimation, the approach of Bansal et al. [77] has been implemented. The contact area has been divided into two parts. The area directly below the tool, in the region below the top of the undeformed sheet, and area above the undeformed sheet as shown in Figure 3.4 (a) and 3.4 (b). The area above the undeformed sheet leaves the contact with the sheet tangentially in the circumferential direction. Let the section XX' is cut and the top sectioned view is shown in the Figure 3.4 (c).

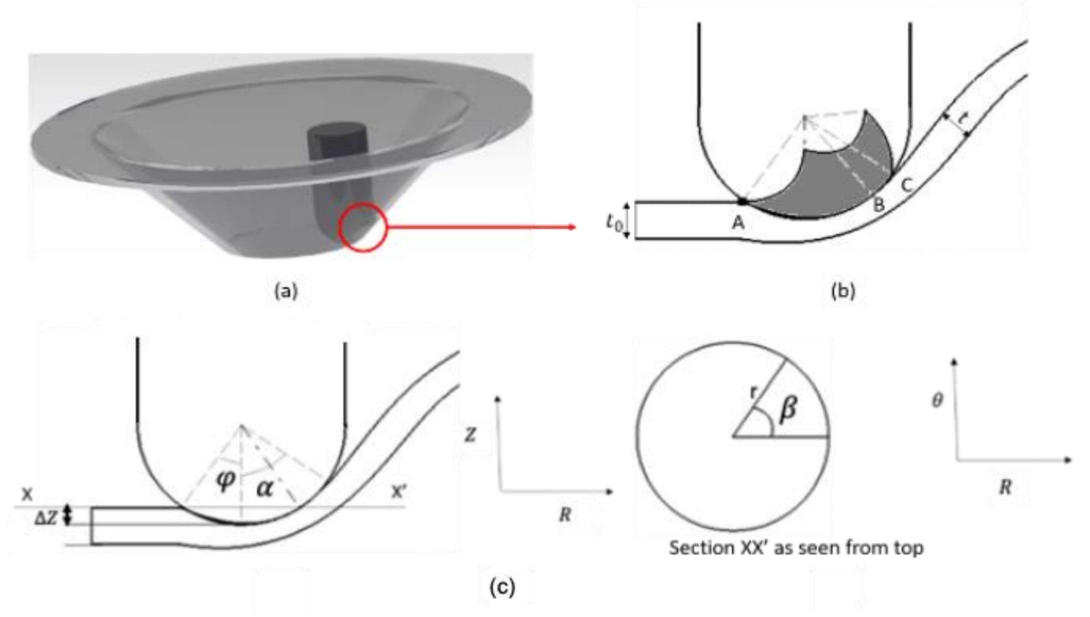

Figure 3.4: (a) 3D view of the contact area, (b) contact area in r-z plane, and (c) top view of section XX'.

From Figure 3.4(c), $\cos\varphi = \frac{R-\Delta Z}{R}$ *(34)*

Area of portion AB can be directly estimated by considering the concept of solid angle. The area can be given by

$$A_{AB} = 2\pi R\Delta Z \tag{35}$$

The area of the portion above the top of the undeformed surface can be given by integrating the perimeters of the strips of width $d\theta$ taken at an angle θ the length of which will be rβ where r = R sinθ

$$A_{AB} = \int PRd\theta = \int R^2\beta \sin\theta d\theta \tag{36}$$

As θ moves from φ to α, β varies from $^{\pi}/_{2}$ to 0

Taking the variation of β to be linear with θ, $(\beta - 0) = \frac{-\pi}{2(\alpha-\varphi)}(\theta-\alpha)$

$$\beta = \frac{\pi}{2(\varphi-\alpha)}(\theta-\alpha) \tag{37}$$

From *(36)* and *(37),*

$$A_2 = \frac{R^2\pi}{2(\varphi-\alpha)}\int_{\varphi}^{\alpha}(\theta-\alpha)\,sin\,\theta\,d\theta \tag{38}$$

$$A_2 = \frac{\pi R^2}{2(\varphi-\alpha)}[sin\,\alpha + (\varphi-\alpha)\,cos\,\varphi - sin\,\varphi] \tag{39}$$

Total area of contact can be given by

$$A_T = \frac{\pi R^2}{2(\varphi-\alpha)}[sin\,\alpha + (\varphi-\alpha)\,cos\,\varphi - sin\,\varphi] + 2\pi R\Delta Z \tag{40}$$

$$A_T = \frac{\pi R}{2}(R+3\Delta z) - \frac{\pi R^2}{2(\alpha-\varphi)}[sin\alpha - sin\,\varphi] \tag{41}$$

Putting R=5 mm, $\Delta z = 0.5$, $\alpha = \frac{\pi}{4}$ and $\varphi = \frac{5\pi}{36}$, $A_T = 19.05$

Considering the whole contact area as a rectangle of $(l \times b)$ $area.$

$l = R(\varphi + \alpha)$ = 6.10 mm and b = 3.11 mm,

length of the portion above the top of the undeformed sheet is $l_{CD} = R(\alpha - \varphi) = 1.75\ mm$

Total projected area in Z-plane = $(Rsin\alpha)b\ sin\alpha = 7.775\ mm^2$ (42)

Total projected area in r-plane =

$$A_r = (\Delta Z + R(cos\varphi - cos\alpha))\,b\,sin\alpha = 3.28\ mm^2 \tag{43}$$

Total projected area in θ-plane = $A_\theta = tl = 4.52\ mm^2$ (44)

Different forces acting on the sheet in contact region can be represented by the force diagram as given in Figure 1.1.

$$F_r = \sigma_{rr} \times A_r + z_{r\theta}A_\theta + z_{rz}A_z \tag{45}$$

$$F_z = \sigma_{zz}A_z + z_{rz}A_r \tag{46}$$

$$F_\theta = \sigma_{\theta\theta}A_\theta + z_{r\theta}A_r \tag{47}$$

Once the relations for various force components were established, the calculation for forces using different developed equations was done on MATLAB for different instantaneous radii. The whole process was modelled on ABAQUS V6.13 and average forming forces were evaluated from FEA model for same instantaneous radii. The values obtained from analytical model were compared with FEA and experimental results, as discussed in subsequent sections.

3.4 Simulation study

The simulation analysis on the formed cone was carried out on ABAQUS V6.13. The finite element model was made on the software which consisted of rigid tool with tool diameter of 10 mm, deformable aluminium alloy 6061 sheet of thickness 1.05 mm and flange to hold the sheet. The geometry of the model used for simulation has been given in Figure 3.5(a)-(c)

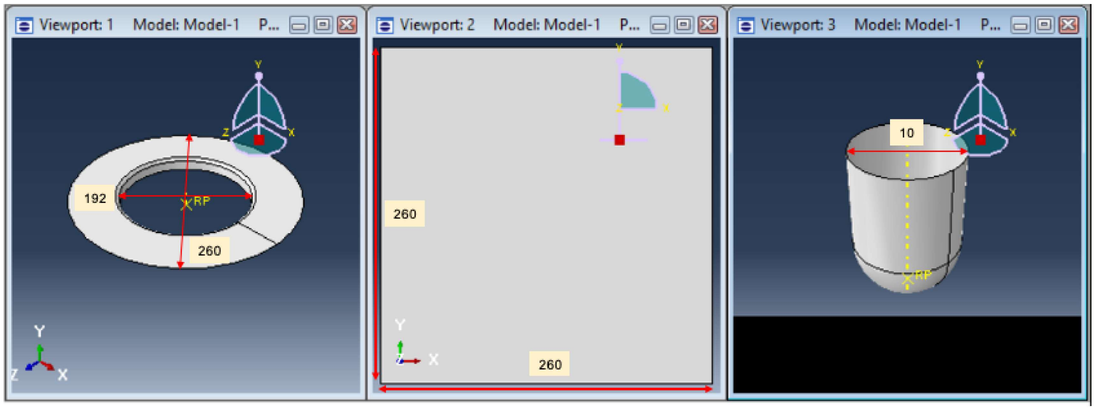

(a) (b) (c)

Figure 3.5: Parts used in ABAQUS V6.13 with dimensions in mm: (a) Tool holder, (b) Sheet, and (c) Forming tool [19].

The properties of the material used in the simulation were obtained from uniaxial tensile test and are presented in Table 3.1.

Table 3.1: Details of parameters used for simulation on ABAQUS V6.13

Properties used in Simulation	Corresponding Values
0.2% offset yield strength (MPa)	111.6
UTS(MPa)	118.2
Elongation	16.1%
Strength coefficient	205 MPa
Strain hardening exponent	0.2
Coefficient of Friction between tool and blank	0.2
Hardening model used	Isotropic
Mesh size	6.96 mm
Mesh type	Square
No of elements taken	101 x 101
Simulation run time	28 Hours

For simulation, true stress-true strain curve up to maximum load was obtained from tensile test. Since large strain is obtained in ISF, for post necking values of true stress and true strain, following method was adopted. The log-log plot of true stress and true strain was made till the onset of necking. Thereafter, linear relation was assumed between logarithm of true stress and logarithm of true strain from necking to fracture. The strain hardening exponent in this region can be evaluated by finding slope of this linear portion of plot from necking to fracture. In this way the true stress- true strain data were obtained and fed in ABAQUS till fracture. The engineering and true stress-strain curve obtained from tensile testing is given in Figure 3.6.

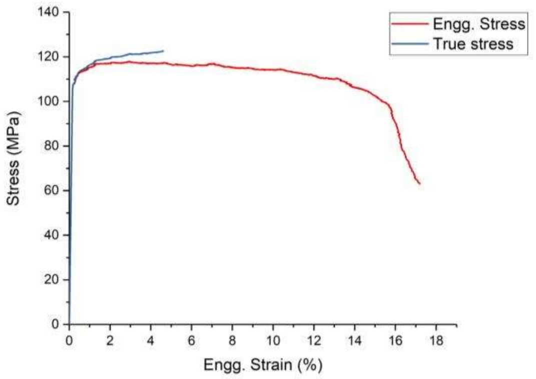

Figure 3.6: Engineering and true stress and strain curve of the Aluminium 6061 alloy.

Isotropic hardening model was used for analysis as the sheet was annealed. Square meshing was done on the plate and tool with average mesh size of 6.96 mm.

3.5 Loading and boundary condition

Penalty contact between tool and sheet has been taken with the coefficient of friction between tool and the sheet to be 0.2 which has obtained from wear test. The boundary of the sheet has been encastred and the blank has been made rigid and encastred. The tip of the tool is chosen as reference point and was given corresponding motions as per the conical geometry. The tool path has been generated on MATLAB and the corresponding positions have been fed in ABAQUS to obtain the conical shape. The simulation has been run and dynamic analysis was done for stresses, strains, and tool forces arising during the tool motion, the results of which are given in Figure 3.7(a), (b) and (c) respectively.

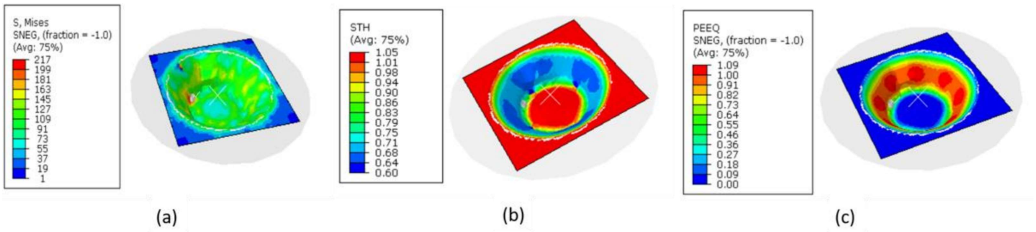

Figure 3.7: Simulation results of formed part on ABAQUS: (a) Stress distribution (MPa) in the deformed cone, (b) Strain distribution in the deformed cone, and (c) Thickness variation (mm) within the deformed cone.

As can be seen from Figure 3.7(a), the Von-Mises stress is maximum in the direct contact region between the undeformed sheet and the tool. The middle region of the cone is strained to the maximum value as can be seen from Figure 3.7 (b). Further, it can also be seen from Figure 3.7 (c) that the middle region of the cone has the minimum thickness showing that this region has undergone the maximum amount of thinning which also affirms the distribution as seen in 3.7 (b). A path along the central meridional plane was chosen in the cone after deformation and strain occurred along the path and thickness of the sheet along the path was plotted, which is shown in Figure 3.8 (a) and 3.8 (b) respectively.

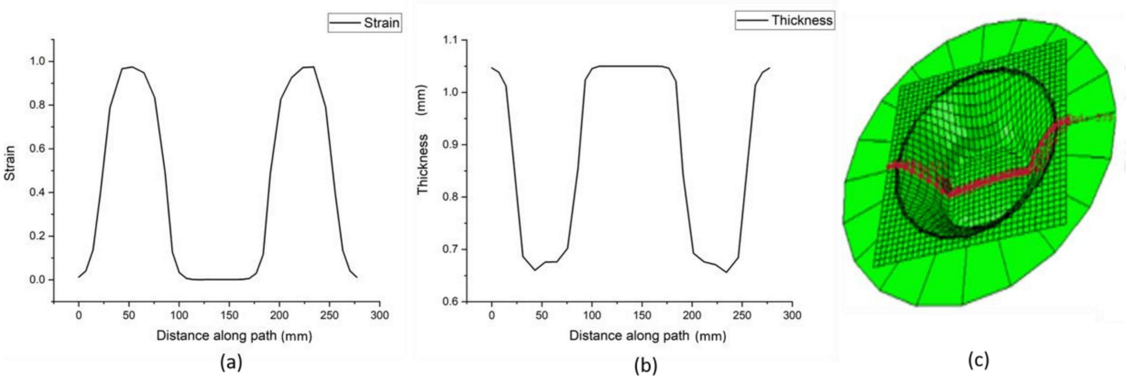

Figure 3.8: (a) Strain vs. true distance along the path, (b) true thickness vs. true distance along the path, and (c) chosen path.

The simulation analysis has been used to find out the forces acting on the tool during the deformation. The tool force has been assumed to have two components. The axial components of the force F_{zz}, and the resultant of the component forces in planes X and Y which is also equal to resultant of tangential and radial force components.

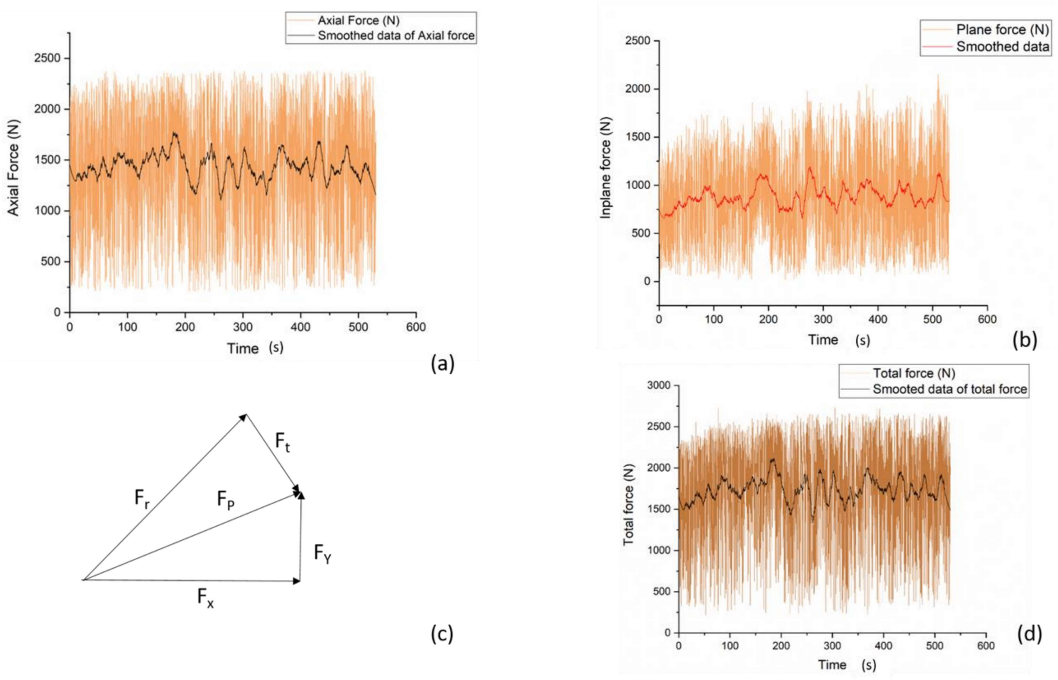

Figure 3.9: (a) Axial force with smoothened curve, (b) in plane force with smoothened curve, (c) decomposition of plane forces, and (d) total force with smoothened curve.

It can be seen from Figure 3.9 that the largest force component arising during the deformation is in the axial direction, as also reported by Duflou et al. [69]. Additionally, it is observed that largest axial force appearing in the axial direction was found to be 2629.11 N. The mean force is found to be 1512.24 N. The variation of in plane force, that is the resultant of the forces appearing in the plane of undeformed sheet with time has been shown in Figure 3.9 (b) and the force diagram for the same has been displayed in Figure 3.9 (c). The largest value corresponding to in plane forming force is found to be 2172.31 N and the average force during forming is found to be 1109.3 N. Finally, the variation of total forming force with time has been shown in Figure 3.9 (d). The maximum forming force appearing on the tool is found to be 2747.46 N and the average of tool force was 1812 N.

3.6 Experimental validation

Once the analytical model was developed and force calculations were done, simulation was carried out for preliminary validation of obtained forces analytically, finally experiments were carried out on six axis industrial robotic arm. 1.05 mm thick aluminium 6061 alloy sheets have been taken for experimentation the details of which is given in section 2.5 of chapter 2.

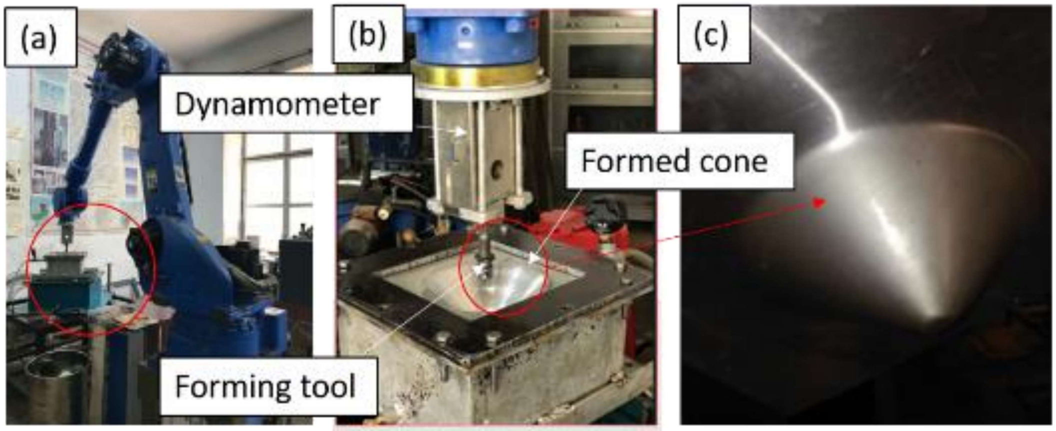

Figure 3.10: (a) Setup with tool dynamometer, (b) tool used for sheet deformation, (c) deformed sheet.

After obtaining the mechanical parameters from the uniaxial tensile test and Erichsen cup test, experiments have been performed for which the chosen parameters are given in Table 3.2. The parameters have been obtained using surface regression models. Dimension of the undeformed work piece is taken as 250 mm x 250 mm x 1.05 mm. The sheet has been deformed into cone with radius of the top circle 96 mm. The whole setup, forming tool with tool dynamometer and deformed axis symmetric cone has been shown in Figure 3.10 (a), (b) and (c) respectively.

Table 3.2: Various parameters used for forming axis symmetric cone.

Parameters	Corresponding values
Tool speed	200 mm/sec
Tool diameter	10 mm
Step depth	0.5 mm
Initial circle radius	96 mm
No of cycles run	100
Measured depth of cone	47.6 mm
% spring back	4.8%

3.7 Results and discussions

3.7.1 Thickness distribution

The instantaneous thickness has a role to play in equation no 18; hence, the state of stress and the force are affected by the instantaneous sheet thickness, so the value of the sheet thickness was obtained from the FEA model and was validated by measuring the values after the experiments.

Once the experiments have been carried out, the thickness of the sheet is measured the sheet was cut meridionally using wire electro-discharge machining (W-EDM) as shown in Figure 3.11(a). The measurement has been done by micrometer with conical tips of least count 0.001 mm. The sheet is found to have the minimum thickness in the middle of the cone. The trend has been also shown in the previous work of Ambrogio et al. [138], who showed that the thickness prediction by the sine law is most accurate in middle region of the deformed sheet. The conical region has been divided into seven sub-regions (0-6) as shown in Figure 3.11 (a) and the thickness in the different regions has been measured. Region-0 is the un-deformed region where thickness is 1.05 mm and region-6 are the lower undeformed region. However, region 1-5 is the region in which sheet thinning can be predicted by sine law. For thickness prediction using FEA analysis, a path has been chosen in the meridional direction, as shown in the fig 3.11(b). The thickness variation obtained from FEA is shown in fig 3.11(c). All the three thickness variations; obtained experimentally, by FEA, and by sine law [4] are plotted along the meridional path as shown in Figure 3.11(b).

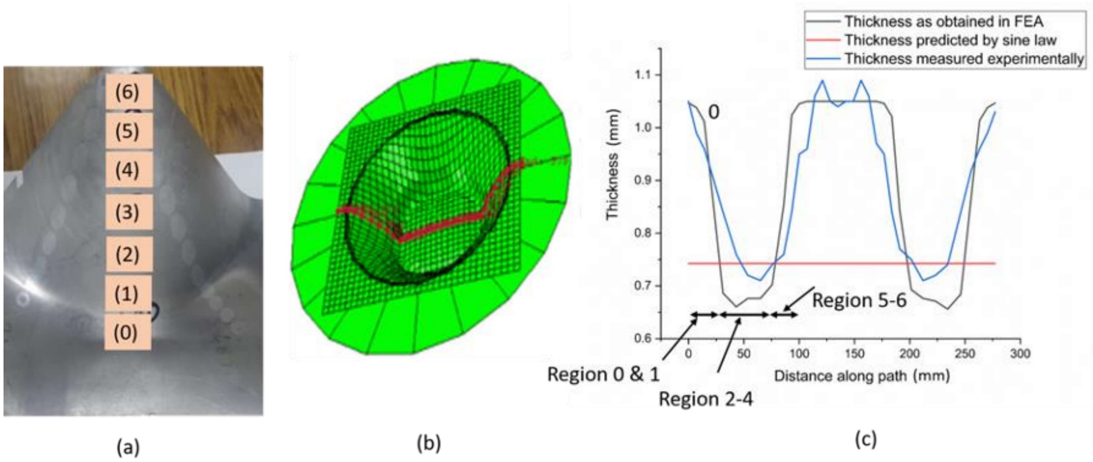

Figure 3.11 : (a) Different regions defined on the formed cone, (b) path chosen on formed cone in FEA model, and (c) thickness variation evaluated experimentally, by FEA model and by sine law.

3.7.2 Force measurement

The force has been measured during deformation using drill tool dynamometer with 3D load cell. The setup is shown in Figure 3.10(a) and (b). The capacity of the dynamometer is 500 kgf having strain gauge based 350 Ω bridge sensor. The force has been measured in X, Y, and Z directions, and the resultant of the forces in X and Y directions has been calculated. Three forces are defined as F_z, F_p (resultant of forces in X and Y directions) and total force (F_t). Average values of F_z, F_p, and F_t calculated for one complete cycle and were compared with the values obtained analytically. For comparison with the forces obtained from simulation analysis, the average of forces for one complete circular cycle has been calculated. Thus, all the components of forces are obtained from analytical model as well as FEA model using ABAQUS and final validation has been done by experimental results. The corresponding values of forces have been plotted against the values of instantaneous radius of the cone.

3.7.2.1 Variation of axial force

This force acts in the vertical direction. The force has been calculated via analytical model as well as FEA model. Both have been validated using final experimentation. The peak and the average values of the axial forces obtained in all three cases are given in Table 3.3.

Table 3.3 : Comparison of peak forces and average forces obtained analytically, by FEA model, and determined experimentally.

Model	**Average value (N)**	**Peak value (N)**
Analytical	1863.45	1957.15
FEA	1876.69	1997.01
Experimentation	1802.21	1963.41

The axial force increased with decreasing radius as observed in the analytical model. The force in the axial direction is given by $F_{zz} = \sigma_{zz} A_z + z_{rz} A_r$. The values of forces have been calculated for different radii of the undeformed sheet using the formula, and the force is found to increase with decreasing radius. The variation of the axial force with decreasing radii is found to be almost linear. The same trend has been seen from the FEA model and also experimentally it is seen to increase with decreasing radii but the shape of the plot departed from linearity slightly in the middle zone, as shown in Figure 3.12 (a) and 3.12 (b). This can be due to sheet thinning which gives rise to inaccurate sheet thickness at different points for a given radius. Nevertheless, the model gives a very good approximation of axial forming force during deformation. The error function of the forces obtained analytically is defined as

$$Percentage\ error = \frac{F_{analytical} - F_{experimental}}{F_{experimental}}\ x\ 100 \qquad (48)$$

The maximum error was found to be 4.92 %. The trend of the force as observed in ABAQUS, also closely matched the data obtained experimentally. The maximum error obtained in this case was 5.52 %. The error in the axial force with respect to the experimental force calculated at every value of radius is shown in Figure 3.15 (a).

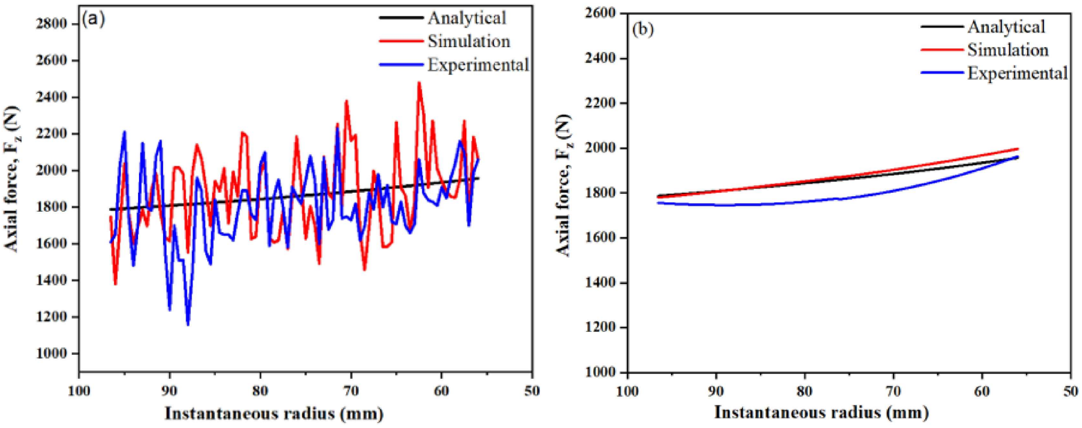

(a) (b)

Figure 3.12: (a) Variation of axial force and (b) fit curve of axial force with instantaneous radius of the undeformed sheet as observed from mathematical model, FEA, and experiments

3.7.2.2 Variation of resultant force in r-θ plane

The force in r-θ plane has two components. For the mathematical model, the two components of forces evaluated are the ones in r and θ planes. However, the components of the forces measured by the dynamometer and the forces observed in the ABAQUS analysis are in X and Y directions, so the resultant of F_r and F_θ has been calculated which is equal to the resultant of F_X and F_Y. Finally, the force obtained analytically and that obtained by FEA have been compared with the experimental force. The peak and the average values of the resultant force in r-θ obtained in all three cases are given in Table 3.4.

Table 3.4: Comparison of peak and average forces resultant force in r-θ plane obtained analytically, by FEA model, and determined experimentally.

Model	**Average value (N)**	**Peak value (N)**
Analytical	1538.63	1597.54
FEA	1526.26	1570.94
Experimentation	1493.88	1509.53

The plots of forces obtained in r- θ plane from analytical model, FEA and experimentally is given in Figure 3.13 (a) and (b). The force obtained analytically had good level of accuracy with experimental force. The largest error is found to be 8.47 % and the force obtained on FEA is found to have a maximum deviation of 4.61 % from the values measured experimentally. The error in the axial force with respect to the experimental force calculated at every value of radius is shown in Figure 3.15 (b).

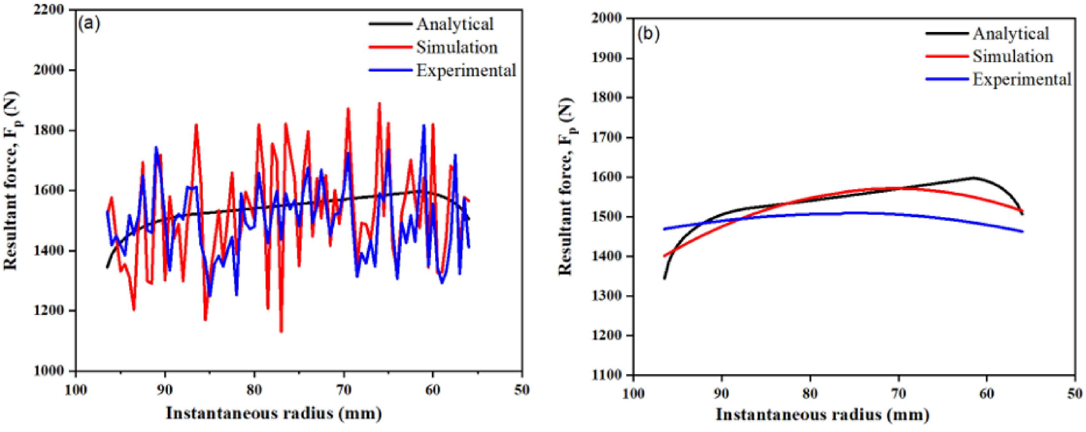

(a) (b)

Figure 3.13: (a) Variation of F_p and (b) fit curve of F_p with instantaneous radius of the undeformed sheet as observed from mathematical model, FEA, and experiments.

3.7.2.3 Variation of total force

In the analytical model, the total force appearing on the forming tool-sheet interface has been calculated by the formula $F_t = \sqrt{{F_p}^2 + {F_z}^2}$. Once the force was calculated, it has been compared with the total force obtained experimentally and the one obtained by the FEA model. The peak and the average values of the total force obtained in all the three cases are presented in Table 3.5.

Table 3.5: Comparison of peak and average value of total forces obtained analytically, by FEA model, and determined experimentally.

Model	**Average value (N)**	**Peak value (N)**
Analytical	2416.70	2504.13
FEA	1526.26	1570.94
Experimentation	1493.88	1509.53

The plots of total force obtained analytically, by FEA model and experimentally are shown in Figure 3.14 (a) and (b). The computed axial force from the mathematical model has good level of accuracy as far as the total force is concerned. The maximum error in the calculated force from the experimental total force was found to be 4.25 %.

The total force has been also obtained from the FEA model on ABAQUS. The force obtained from FEA model also was in close agreement with the total force obtained experimentally. The maximum error in the obtained total force by FEA model from that determined experimentally was found to be 4.89 %, as shown in Figure 3.15 (c).

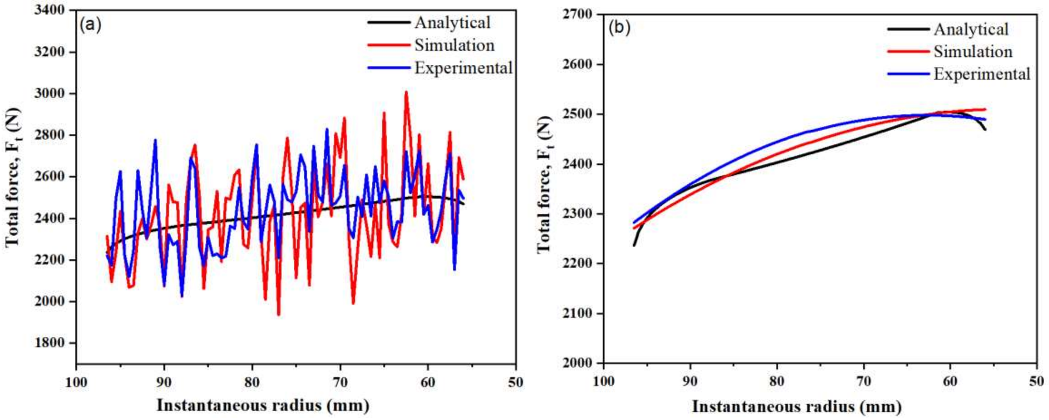

Figure 3.14: (a) Variation of total force and (b) fit curve of total force with instantaneous radius of the undeformed sheet as observed from mathematical model, FEA, and experiments.

3.7.2.4 **Error in calculated and experimentally determined forces**

The forces calculated from analytical model have been compared with forces obtained by FEA model and experimentally. For validation purpose the true value of force has been taken as the one which has been obtained experimentally. The values of the forces have been obtained from analytical model for different instantaneous radii and the corresponding values of the forces have also been obtained from ABAQUS data. Both the values have been compared with experimental values; thus, validation of the mathematical model has been done comparing the values of the forces with the experimental values.

The error function has defined as percentage error =

$$\frac{F_{calculated} - F_{experimental}}{F_{experimental}} \; x \; 100$$

For axial forces and the total forces, the error was maximized in the zone 2 i.e., the middle region of the cone. However, for the resultant force in r-θ plane, the error was maximum in the region 1 which decreased and then error was increased in region 2 before finally decreasing in the region 3.

As far as the FEA model is concerned, the validation was done by comparing the forces obtained experimentally. The error for all three forces followed the same trend. The percentage error vs. instantaneous radius followed a bell curve pattern. It maximized in the region 2 and was minimal in region 1 and region 3. The error curves are given in Figures 3.15 (a), (b), and (c).

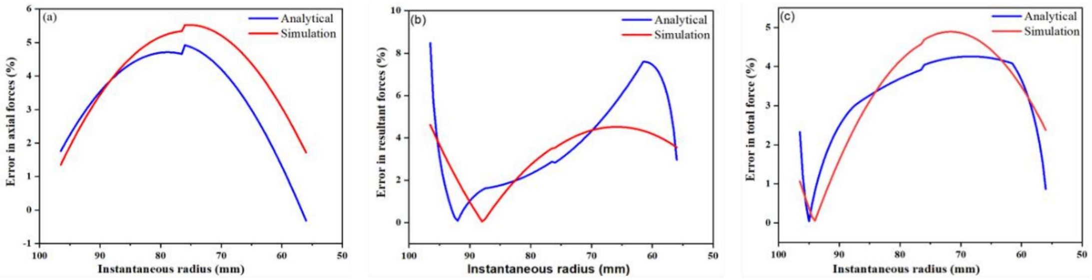

(a) (b) (c)

Figure 3.15: Percentage error in: (a) axial force, (b) resultant force, and (c) total force.

3.8 Conclusions

This chapter presented an analytical model to predict the forming forces during incremental sheet forming. The modeling was done in a polar 3D coordinate system. All six stress components have taken into consideration initially before neglecting $\tau_{\theta z}$. Analytical formulae have developed for all the stress components. The contact area has been modeled analytically before finally developing the equations for all forces. The three force components for which the equations have been developed are F_r, F_θ, and F_z. The result of the three components is the total force F_t. The resultant of F_r and F_θ is the resultant force in the r-θ plane, represented as F_p. The material used in the mathematical model was AA6061. The process has been modeled in FEA using the same experimental parameters, and the force components F_z and F_p have been calculated before finally calculating the total force (F_t). Finally, the process has been carried out on a six-axis industrial robot, and forces have been measured using a tool dynamometer. The data obtained from the analytical model and

FEA have been validated by the experimental results. The model is for all wall angle cones; however, in this work, the validation has been done for a 45° cone. The results obtained from the analytical model and FEA are found to be in good agreement with the experimental result. The maximum error in the analytically calculated total force is found to be 4.25%. Similarly, the results obtained from the FEA model are also in agreement with the experimental results. The maximum error in evaluated total force from the FEA model is found to be 4.89% with respect to the experimental results. It can be concluded that the mathematical model developed can be used for a force calculation to a good level of accuracy.

The next chapter deals with new class of RAISF i.e., RAISF with fluid pressure from back. The process has been termed as Robot Assisted Incremental Sheet Hydroforming (RAISHF). In order to check the feasibility of the process, a comparison has been made between RAISF and RAISHF as given in next chapter.